

# Characterizations of Single-Crystal Lithium Niobate Thin Films

Qingyun Li, Honghu Zhang, Houbin Zhu and Hui Hu \*

State Key Laboratory of Crystal Materials, School of Physics, Shandong University, Jinan 250100, China; liqingyun@mail.sdu.edu.cn (Q.L.); hhzhang@mail.sdu.edu.cn (H.Z.); zhuhoubin@nanoln.com (H.Z.)

\* Correspondence: hhu@sdu.edu.cn

**Abstract:** Single-crystal lithium niobate thin films (lithium niobate on insulator, LNOI) are becoming a new material platform for integrating photonics. Investigation into the physical properties of LNOI is important for the design and fabrication of photonic devices. Herein, LNOIs were prepared by two methods: ion implantation and wafer bonding; and wafer bonding and grinding. High-resolution X-ray diffraction (HRXRD) and confocal Raman spectroscopy were used to study the LNOI lattice properties. The full-width at half-maximum (FWHM) of HRXRD and Raman spectra showed a regular crystal lattice arrangement of the LNOIs. The domain inversion voltage and electro-optical coefficient of the LNOIs were close to those of LN bulk material. This study provides useful information for LNOI fabrication and for photonic devices in LNOI.

**Keywords:** lithium niobate thin films; crystal lattice; domain inversion voltage; electro-optical coefficient

## 1. Introduction

Lithium niobate (LN) is one of the most attractive materials in integrated photonics, owing to its many excellent physical properties [1,2]. Classical LN photonic devices are usually based on low refractive index waveguides formed by proton exchange and titanium diffusion [3–5]. These devices have weak optical mode confinement, which greatly limits their application in integrated photonics. Single-crystal lithium niobate thin film (lithium niobate on insulator, LNOI, or thin film lithium niobate, TFLN) retain the excellent physical properties of LN bulk material and exhibit a high refractive index contrast [6,7]. In the past few years, with the development of LNOI preparation technology and the breakthrough of micro-fabrication technology, high performance and highly integrated photonic devices have been reported [8–10].

The study of LNOI physical properties is important for the design and fabrication of integrated optical devices. There are few reports on the physical properties of LNOI fabricated by ion implantation and wafer bonding (smart-cut or ion-cut). The refractive index and crystal lattice of LNOI have been reported [11]. The modulation efficiency of LN electro-optic devices depended strongly on the electro-optic (E-O) coefficient. The E-O coefficient of the proton exchange waveguide in LNOI has been studied [12]. The proton exchange process was able to change the E-O property, which added some uncertainty to the E-O coefficient measurement. Domain polarization inversion is an important process for nonlinear optics employing quasi-phase-matching. Domain inversion voltage is essential for fine, smooth, and perfect periodic polarization structure [13]. Various domain inversion structures have been realized on LNOI, and the domain inversion voltage of LNOI was found to be higher than that of LN bulk materials [14–16]. It is speculated that the reasons were the  $\text{Li}^+$  out-diffusion during annealing processes and the interface between the LN thin film and the  $\text{SiO}_2$  layer [15,16]. However, the relationship between domain inversion voltage and annealing temperature has not been clarified. In addition, LNOIs were able to be fabricated by wafer thinning technology (such as ion milling or direct grinding/polishing) [17–21], which could avoid the crystal lattice damage caused by the ion implantation process [22]. Micro-disk and micro-ring resonators have been



**Citation:** Li, Q.; Zhang, H.; Zhu, H.; Hu, H. Characterizations of Single-Crystal Lithium Niobate Thin Films. *Crystals* **2022**, *12*, 667. <https://doi.org/10.3390/cryst12050667>

Academic Editor: Shujun Zhang

Received: 5 April 2022

Accepted: 30 April 2022

Published: 6 May 2022

Corrected: 19 December 2022

**Publisher's Note:** MDPI stays neutral with regard to jurisdictional claims in published maps and institutional affiliations.



**Copyright:** © 2022 by the authors. Licensee MDPI, Basel, Switzerland. This article is an open access article distributed under the terms and conditions of the Creative Commons Attribution (CC BY) license (<https://creativecommons.org/licenses/by/4.0/>).

demonstrated with Q factors beyond  $10^8$ , which approaches the intrinsic material absorption limit of LN [18,19]. Many frequency conversions have been observed in ultrahigh-Q micro-resonators. For example, second harmonic generation (SHG), third harmonic generation (THG), fourth harmonic generation (FHG), and optical parametric oscillation (OPO). The interface between LN thin film and substrate, surface roughness, and bonding strength of LNOI with thicknesses of several micrometers have been investigated [20,21]. However, the physical properties of submicron-thick LNOI fabricated by wafer thinning technology have rarely been reported.

In this study, the lattice properties, domain inversion voltage, and E-O coefficient of LNOIs were investigated. First, we characterized the LNOI fabricated by wafer bonding and grinding. The FWHM of the (110) plane measured by HRXRD was  $0.027^\circ$  and the FWHM of the Raman spectrum at  $153\text{ cm}^{-1}$  was  $9.41\text{ cm}^{-1}$ , which shows a regular lattice arrangement. The domain inversion voltage of LNOIs measured by multiple electric pulses was  $20.4 \pm 0.9\text{ kV/mm}$ , which is close to that of bulk material. The E-O coefficient of LNOI was  $27.3 \pm 0.4\text{ pm/V}$ , which is also close to that of bulk material. Second, we characterized the LNOIs fabricated by ion implantation and wafer bonding. After annealing at high temperature, their properties were found to be similar to those of LNOIs fabricated by wafer bonding and grinding. This study provides useful information for LNOI fabrication and for photonic devices in LNOI.

## 2. Experiments

The LNOIs were prepared by two methods: ion implantation and wafer bonding, and wafer bonding and grinding. The process with ion implantation and wafer bonding is described in Ref [7]. The He ion energy was 250 keV with a dose of  $4 \times 10^{16}\text{ ions/cm}^2$ , and an x-cut LNOI with a thickness of 700 nm was fabricated. The LNOI was annealed at  $350\text{ }^\circ\text{C}$  (LNOI annealing at  $350\text{ }^\circ\text{C}$ ) or  $500\text{ }^\circ\text{C}$  (LNOI annealing at  $500\text{ }^\circ\text{C}$ ) to repair lattice damage caused by ion implantation. The process of fabricating LNOI by wafer bonding and grinding (grinded LNOI) is shown in Figure 1. First, a layer of  $\text{SiO}_2$  was grown on an Si substrate by thermal oxidation, and the  $\text{SiO}_2$  was polished to a suitable thickness (2 microns) by chemical mechanical polishing (CMP). Then, an x-cut LN wafer was directly bonded to the Si substrate. Next, the LN crystal was grinded to a suitable thickness and CMP was used to reduce the surface roughness of the thin film to less than 0.5 nm. Finally, an x-cut LNOI with a thickness of 700 nm was fabricated, which could avoid lattice damage caused by the ion implantation process. High-resolution transmission electron microscope (HRTEM) was used to investigate the interface and crystal lattice of the grinded LNOI. Figure 2a shows a TEM image in which the LNOI structure is clearly seen. Figure 2b shows a high-magnification TEM image, with a clear film interface between LN and  $\text{SiO}_2$  and an ordered lattice arrangement of LN.

HRXRD with  $\text{Cu K}\alpha_1$  ( $\lambda = 1.54056\text{ \AA}$ ) as the X-ray radiation source was used to investigate the lattice properties of the LNOI. First,  $\omega$ ,  $\psi$  and  $\chi$  scans were used to find the (110) crystal plane of the LNOI, and then an  $\omega$ - $2\theta$  scan with a step of  $0.0012^\circ$  was used to measure the diffraction peak of the LNOI. Confocal Raman spectroscopy was used to investigate the LNOI as well. A 473 nm laser beam was focused onto the surface of the LN thin film through a  $100\times$  objective lens ( $\text{NA} = 0.9$ ), achieving a depth resolution of approximately 320 nm. Raman probing was performed using an 1800 lines/mm grating, achieving a spectral resolution of  $0.69\text{ cm}^{-1}/\text{pixel}$ . Multiple electric pulses were used to study the domain polarization inversion of the LNOI [14]. The domain polarization inversion was achieved by applying high voltage pulses to the metal electrode deposited on the LNOI. As shown in Figure 3a, a 100-nm-thick Cr electrode was deposited on an x-cut LN thin film with a thickness of 700 nm. Figure 3b shows the scheme of the domain polarization inversion configuration. The pulse period and duty cycle were 0.1 s and 50%, respectively. The number of pulses was 20. The direction of the electric field was along the z axis of the LN thin film. The sample was put in silicone oil to avoid air breakdown

caused by the high electric field strength. Piezoresponse force microscopy (PFM) was used to observe the inversion domains.

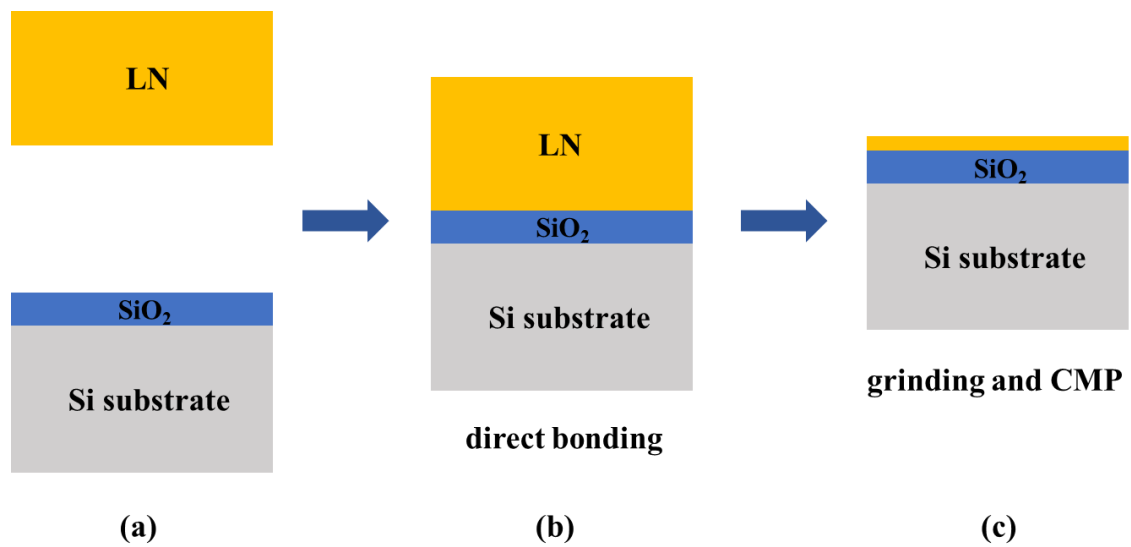


**Figure 1.** Fabrication process of grinded LNOI. (a) A layer of SiO<sub>2</sub> was grown on an Si substrate. (b) Si substrate and LN were directly bonded. (c) LN crystal was grinded and polished.

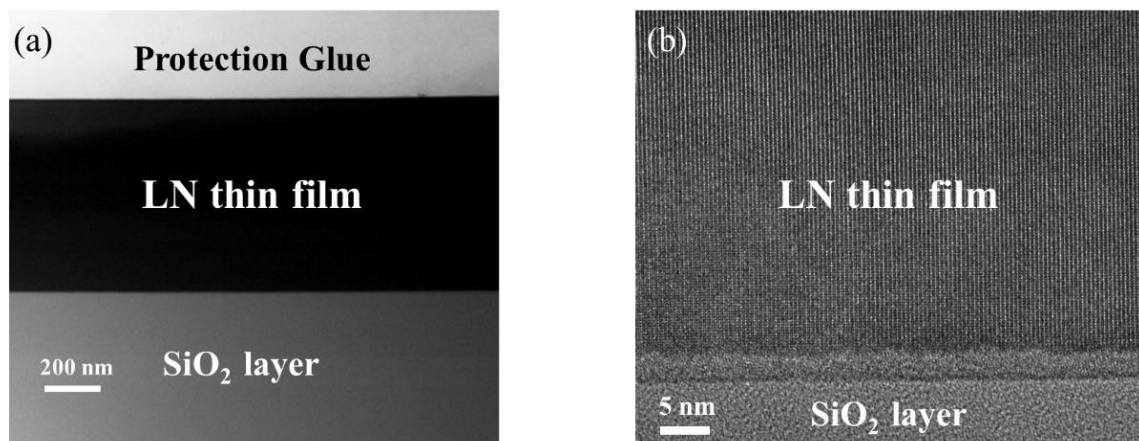


**Figure 2.** Cross section of grinded LNOI observed by TEM (a) and high-magnification TEM (b).

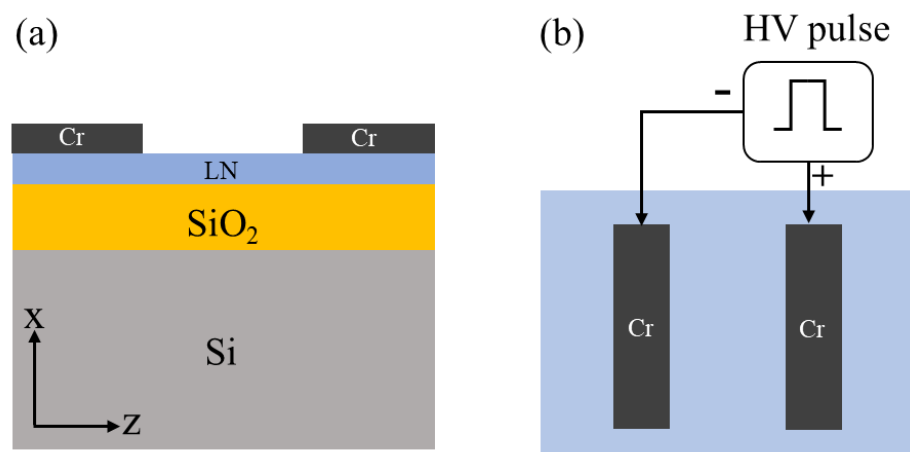


**Figure 3.** Cross section of Cr on x-cut LNOI (a) and scheme of domain polarization inversion configuration (b).

A waveguide phase modulator was fabricated on the LNOI to measure the E-O coefficient  $r_{33}$ . The LN thin film was x-cut and the TE light traveled along the y axis. The two polished end faces of the waveguide formed a low-finesse Fabry–Perot cavity [23]. By applying a continuously varying voltage to the electrodes on either side of the waveguide, the output light intensity will oscillate. The relationship between the half-wave voltage length product  $V_{\pi}L$  and  $r_{33}$  is expressed as follows [24,25]:

$$V_{\pi}L = \frac{n_{eff}\lambda G}{n^4 r_{33} \Gamma} \quad (1)$$

where  $G$  and  $L$  are the gap and length of the electrodes, respectively.  $\lambda$  is the wavelength,  $n_{eff}$  is the effective index of the waveguide, and  $n$  is the extraordinary refractive index of LN. The  $\Gamma$  (overlapping factor) is defined as follows:

$$\Gamma = \frac{G \iint E_{ele}(x, z) |E_{opt}(x, z)|^2 dx dz}{V \iint |E_{opt}(x, z)|^2 dx dz} \quad (2)$$

where  $V$  is the voltage applied to the electrode,  $E_{ele}$  is the electrostatic field, and  $E_{opt}$  is the optical field. The measurement setup is shown in Figure 4. Polarized light with a wavelength of 1550 nm was emitted from a tunable semiconductor laser (Santec TSL-210). The laser beam was coupled into the waveguide by a polarization-maintaining (PM) fiber, and the output light was collected by a 40×/0.65 objective lens and displayed in an oscilloscope by an InGaAs detector. The electrical signal from the waveform generator was applied to the electrode to modulate the light signal in the waveguide. The electrostatic field ( $E_{ele}$ ) and optical field ( $E_{opt}$ ) were simulated by Charge Solutions and Mode Solutions, respectively.

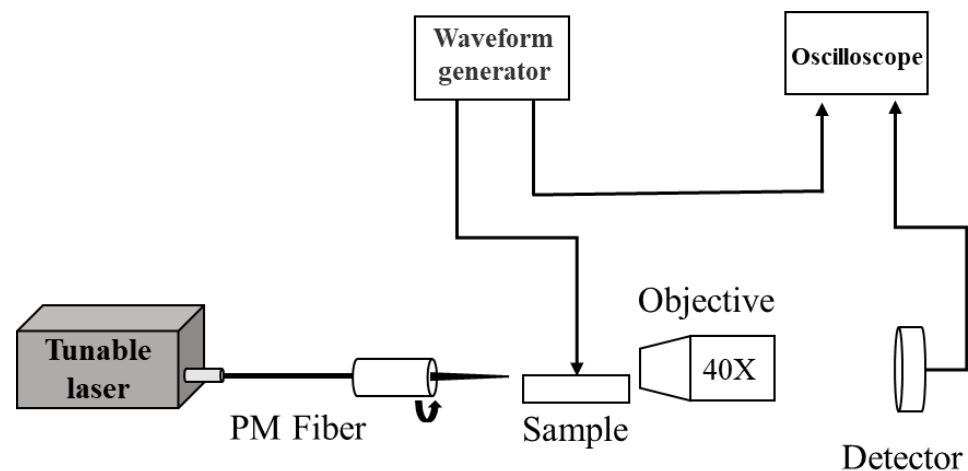
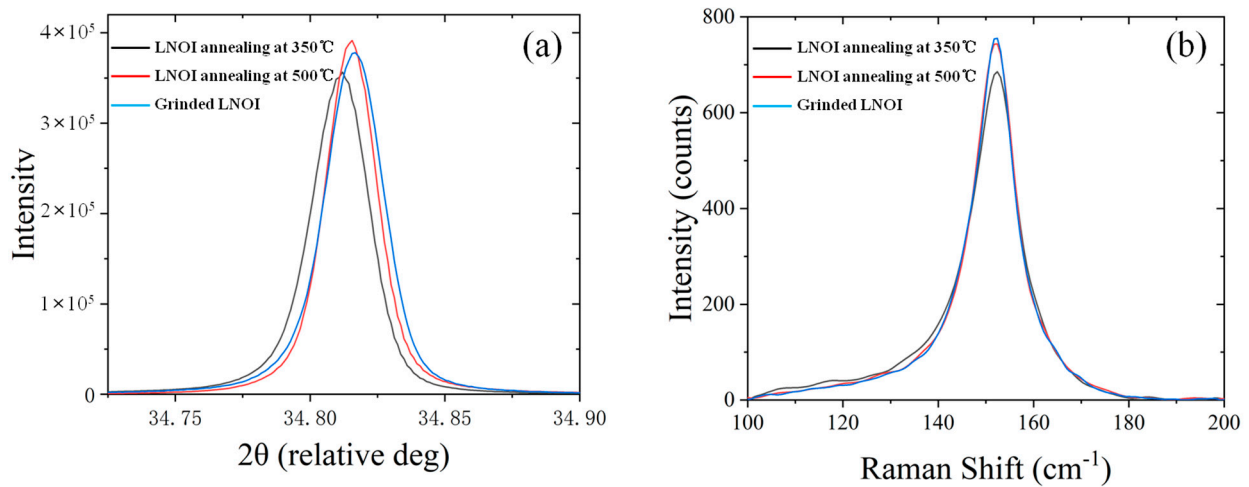


Figure 4.  $V_{\pi}$  measurement setup.

### 3. Results and Discussion

Figure 5a shows the diffraction peaks of the (110) crystal planes of the LNOI as measured by HRXRD. The black line from LNOI annealing at 350 °C had a diffraction peak of 34.809° and a FWHM of 0.026°. The red line from LNOI annealing at 500 °C had a diffraction peak of 34.815° and a FWHM of 0.026°. The blue line from grinded LNOI had a diffraction peak of 34.817° and a FWHM of 0.027°. The FWHMs were small, showing that the LNOI was mono-crystalline with an ordered crystal-lattice arrangement. The FWHM of LNOIs did not show significant differences. To study the lattice structure after undergoing the ion implantation process, Figure 5b shows the polarized Raman spectra of the LNOI at 153  $\text{cm}^{-1}$  with an X(YZ)X scattering configuration. The blue line from the grinded LNOI had a FWHM of 9.41  $\text{cm}^{-1}$ . The black line from the LNOI annealing at 350 °C had a FWHM of 10.75  $\text{cm}^{-1}$ , which was broadened, potentially due to the disorder of the crystal lattice. The red line from the LNOI annealing at 500 °C had a FWHM of 9.41  $\text{cm}^{-1}$ . The FWHM

of LNOI annealing at 500 °C was consistent with that of grinded LNOI, revealing that the crystal lattice of the LN thin film was well recovered without causing an expansion of the frequency range of the lattice vibration.



**Figure 5.** (a) Diffraction peak of LNOI measured by HRXRD. (b) Polarized Raman spectra of LNOI at  $153\text{ cm}^{-1}$ .

The ion implantation process affects the domain inversion voltage of the LNOI. Figure 6 shows the PFM images of domain inversion of LNOI annealing at 350 °C. The areas inside the red frame are the electrodes. The gap between the metal electrodes was  $11.2\text{ }\mu\text{m}$ . As shown in Figure 6a–c, when the voltage was 260 V, there was no domain inversion. When the pulse voltage increased to 270 V, domain inversion was found. Upon increasing the voltage to 280 V, the domain inversion area increased. Figure 6d shows the electrical pulse waveform when the voltage was 270 V. The voltage fluctuation error was 10 V. Therefore, the domain inversion voltage of LNOI annealing at 350 °C was  $270 \pm 10\text{ V}$  ( $24.1 \pm 0.9\text{ kV/mm}$ ). As shown in Table 1, the same method was used to measure the domain inversion voltages of LNOI annealing at 500 °C and grinded LNOI, which were  $20.7 \pm 0.9$  and  $20.4 \pm 0.9\text{ kV/mm}$ , respectively, close to that of LN bulk material ( $\sim 21\text{ kV/mm}$ ). The domain inversion voltage of LNOI annealed at 350 °C is higher than that of LNOI annealed at 500 °C. A possible explanation is that the LN crystal-lattice disorder caused by ion implantation increased the domain inversion voltage. With the increase in annealing temperature, the LN crystal lattice damage was repaired, and the domain inversion voltage decreased.

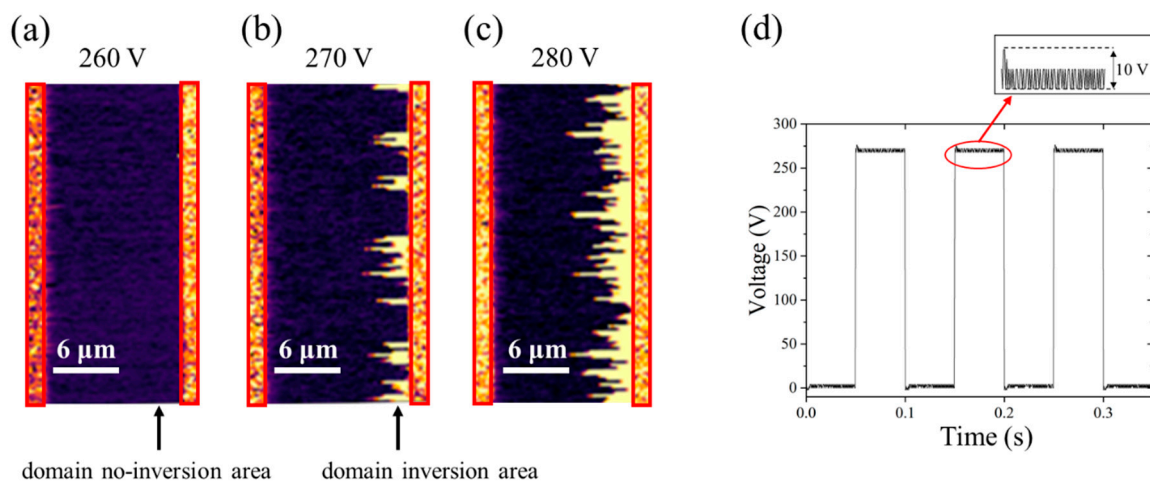
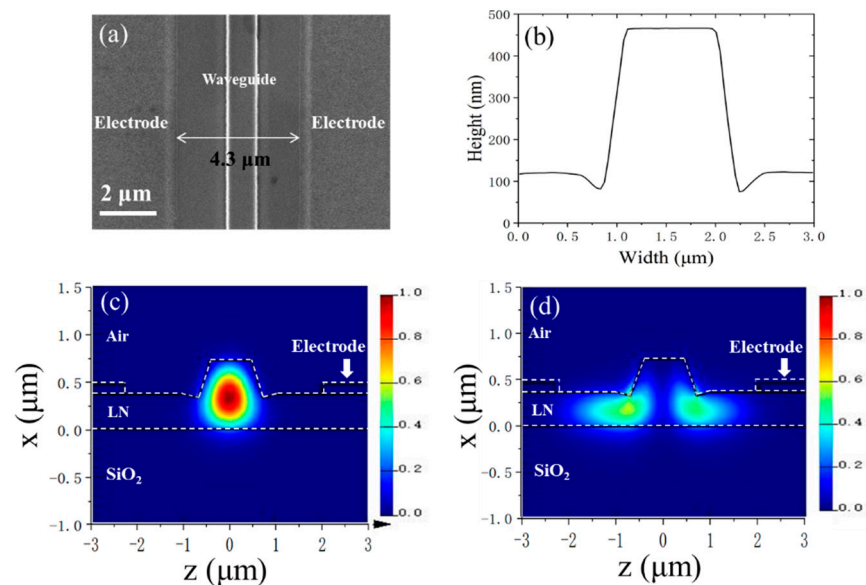


**Figure 6.** Domain inversion images of LNOI annealing at 350 °C at 260 V (a), 270 V (b) and 280 V (c). Electrical pulse waveform when the voltage was 270 V (d).

**Table 1.** The domain inversion voltage of LNOI.

Sample	Domain Inversion Voltage (kV/mm)
LNOI annealing at 350 °C	$24.1 \pm 0.9$
LNOI annealing at 500 °C	$20.7 \pm 0.9$
grinded LNOI	$20.4 \pm 0.9$

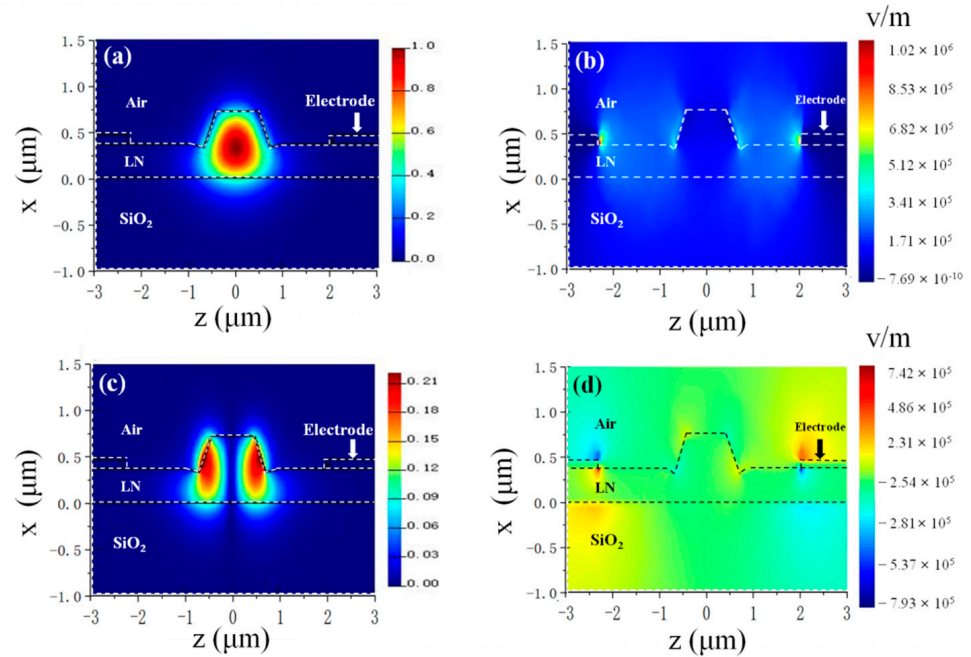
Figure 7a shows a scanning electron microscope (SEM) image of the phase modulator in grinded LNOI. The gap and length of the electrodes were  $4.3 \mu\text{m}$  and  $5 \text{ mm}$ , respectively. Figure 7b shows an atomic force microscope (AFM) image of the LNOI waveguide cross-section. The rib had a top width of  $0.9 \mu\text{m}$  and a bottom width of  $1.4 \mu\text{m}$ . The LN etch depth was  $350 \text{ nm}$ , leaving a  $370 \text{ nm}$  slab (measured by the white light interferometry method). Figure 7c,d show the profiles of the  $\text{TE}_{00}$  and  $\text{TE}_{10}$  mode at  $1550 \text{ nm}$ . When the gap of the electrodes was  $4.3 \mu\text{m}$ , the transmission losses of the  $\text{TE}_{00}$  and  $\text{TE}_{10}$  mode were simulated to be  $0.5$  and  $520 \text{ dB/cm}$ , respectively. Owing to the high transmission loss of the  $\text{TE}_{10}$  mode, the waveguide could be considered to be single-mode transmission. Figure 8a,c show the electric fields  $E_z$  and  $E_x$ , respectively, of the  $\text{TE}_{00}$  mode. Figure 8b,d show the electric fields  $E_z$  and  $E_x$ , respectively, of the electrostatic field after a voltage of  $1 \text{ V}$  was applied to the electrodes. Because the overlapping factors  $\Gamma$  of the  $E_x$  of the  $\text{TE}_{00}$  mode and the  $E_x$  of the electrostatic field were almost 0, their contribution to the phase change of the  $\text{TE}_{00}$  mode can be ignored. The overlapping factors  $\Gamma$  of the  $E_z$  of the  $\text{TE}_{00}$  mode and the  $E_z$  of the electrostatic field were  $0.53$ .



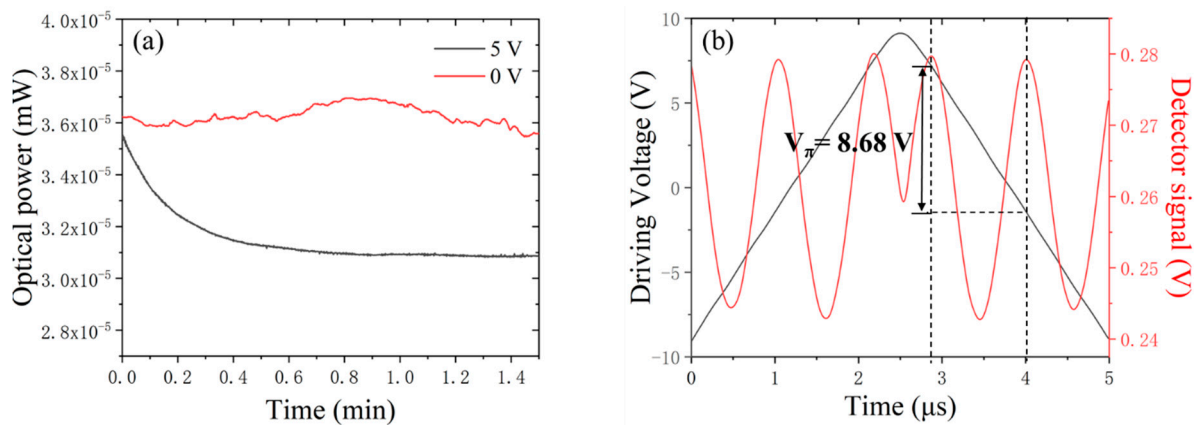
**Figure 7.** SEM image of phase modulator in grinded LNOI (a) and cross-section AFM image of LNOI waveguide (b). Simulated electric field distributions of the  $\text{TE}_{00}$  (c) and  $\text{TE}_{10}$  mode (d) in LN waveguide.

Figure 9a shows the variation of output light power with time after applying volt-ages of  $5$  and  $0 \text{ V}$  on the electrodes. When the voltage was  $0 \text{ V}$ , the output light power was stable with time; when the voltage was  $5 \text{ V}$ , the output light power varied significantly with time. The light power variation was related to the DC bias drift, which resulted from the flow and redistribution of electrical charge in the LN region under DC voltage [26]. This phenomenon would cause uncertainties in the measurement of  $V_\pi$ . Triangular waves ( $200 \text{ kHz}$  with an amplitude of  $18 \text{ V}$ ) were used to minimize the influence of the DC bias drift. Figure 9b shows the measured light transmission at  $1550 \text{ nm}$ . The red and black lines represent the triangular wave electrical and optical signals, respectively, indicating a  $V_\pi$  of  $8.68 \text{ V}$ . The uncertainty of the E-O coefficient mainly results from two aspects. One was the overlapping factor calculation error caused by the uneven morphologies of the

waveguide and electrodes. The other was  $V\pi$  measurement error. The uncertainty of the E-O coefficient was estimated to be within 3%. The E-O coefficient of ground LNOI was  $27.3 \pm 0.4$  pm/V, which was close to that of LN bulk materials (28.6 pm/V [27]). The stress at the interface between LN thin film and SiO<sub>2</sub> might cause the E-O coefficient of LNOI to be smaller than that of LN bulk material [28]. As shown in Table 2, using the same method, the E-O coefficient of LNOI annealing at 350 °C was  $26.1 \pm 0.4$  pm/V, which was lower than grinded LNOI. This might be due to lattice damage caused by ion implantation.



**Figure 8.** Electric field  $E_z$  (a) and  $E_x$  (c) distributions of the TE<sub>00</sub> mode. Electric field  $E_z$  (b) and electric field  $E_x$  (d) distributions of the electrostatic field after 1 V voltage was applied to the electrodes.



**Figure 9.** (a) Variation of output light power with time after applying voltages of 5 and 0 V on electrodes. (b) 200 kHz triangular wave sweep with amplitude of 18 V for 5-mm-long phase modulator. Black line, triangular wave signal; red line, detector signal.

**Table 2.** The E-O coefficients of LN bulk and LNOI ( $\lambda = 1550$  nm).

Material	E-O Coefficient (pm/V)
LN Bulk	28.6
LNOI annealing at 350 °C	$26.1 \pm 0.4$
grinded LNOI	$27.3 \pm 0.4$

#### 4. Conclusions

In conclusion, the lattice properties, domain inversion voltage, and E-O coefficient of LNOIs were studied. For grinded LNOI, the FWHM of the (110) plane of HRXRD was  $0.027^\circ$ , and the FWHM of Raman spectrum at  $153\text{ cm}^{-1}$  was  $9.41\text{ cm}^{-1}$ , revealing a regular lattice arrangement; the domain inversion voltage was  $20.4 \pm 0.9\text{ kV/mm}$ , which was close to that of bulk material. The E-O coefficient of LNOI was  $27.3 \pm 0.4\text{ pm/V}$ , which was close to that of bulk material. After annealing at high temperature, the LNOI fabricated by ion implantation and wafer bonding exhibited properties similar to those of LNOI fabricated by wafer bonding and grinding, which indicated that both methods could produce high-quality LNOIs.

**Author Contributions:** Conceptualization, Q.L. and H.H.; methodology, Q.L.; validation, Q.L.; formal analysis, Q.L. and H.H.; investigation, Q.L.; resources, H.H.; writing-original draft preparation, Q.L.; writing-review and editing, Q.L., H.Z. (Honghu Zhang), H.Z. (Houbin Zhu) and H.H.; data analysis, Q.L.; supervision, H.H.; funding acquisition, H.H. All authors have read and agreed to the published version of the manuscript.

**Funding:** This research is supported by the Natural Science Foundation of Shandong Province, grant number ZR2020LLZ007. Additionally, it is supported by the National Key Research and Development Program of China, grant number 2018YFB2201700 and 2019YFA0705000.

**Data Availability Statement:** Not applicable.

**Conflicts of Interest:** Houbin Zhu is an employee of Jinan Jingzheng Electronics Co., Ltd. (NanoLN, Jinan, China) and involved in developing lithium niobate technologies at NanoLN. Hui Hu is one of the founders of NanoLN and involved in developing lithium niobate technologies at NanoLN.

#### References

1. Weis, R.S.; Gaylord, T.K. Lithium niobate: Summary of physical properties and crystal structure. *Appl. Phys. A* **1985**, *37*, 191–203. [[CrossRef](#)]
2. Arizmendi, L. Photonic applications of lithium niobate crystals. *Phys. Status Solidi A* **2004**, *201*, 253–283. [[CrossRef](#)]
3. Schmid, R.V.; Kaminow, I.P. Metal-diffused optical waveguides in  $\text{LiNbO}_3$ . *Appl. Phys. Lett.* **1974**, *25*, 458–460. [[CrossRef](#)]
4. Bortz, M.L.; Fejer, M.M. Annealed proton-exchanged  $\text{LiNbO}_3$  waveguides. *Opt. Lett.* **1991**, *16*, 1844–1846. [[CrossRef](#)]
5. Jackel, J.L.; Rice, C.E.; Veselka, J.J. Proton exchange for high-index waveguides in  $\text{LiNbO}_3$ . *Appl. Phys. Lett.* **1982**, *41*, 607–608. [[CrossRef](#)]
6. Levy, M.; Osgood, R.M.; Liu, R.; Cross, L.E.; Cargill, G.S.; Kumar, A.; Bakhru, H. Fabrication of single crystal lithium niobate films by crystal ion slicing. *Appl. Phys. Lett.* **1998**, *73*, 2293. [[CrossRef](#)]
7. Poberaj, G.; Hu, H.; Sohler, W.; Gunter, P. Lithium niobate on insulator (LNOI) for micro-photonics devices. *Laser Photonics Rev.* **2012**, *6*, 488–503. [[CrossRef](#)]
8. Qi, Y.F.; Li, Y. Integrated lithium niobate photonics. *Nanophotonics* **2020**, *9*, 1287–1320. [[CrossRef](#)]
9. Zhu, D.; Shao, L.B.; Yu, M.J.; Cheng, R.; Desiatov, B.; Xin, C.J.; Hu, Y.W.; Holzgrafe, J.; Ghosh, S.; Shams-Ansari, A.; et al. Integrated photonics on thin-film lithium niobate. *Adv. Opt. Photonics* **2021**, *13*, 242–352. [[CrossRef](#)]
10. Lin, J.T.; Bo, F.; Cheng, Y.; Xu, J.J. Advances in on-chip photonic devices based on lithium niobate on insulator. *Photonics Res.* **2020**, *8*, 1911. [[CrossRef](#)]
11. Han, H.P.; Cai, L.T.; Hu, H. Optical and structural properties of single-crystal lithium niobate thin film. *Opt. Mater.* **2015**, *42*, 47–51. [[CrossRef](#)]
12. Cai, L.T.; Kang, Y.; Hu, H. Electric-optical property of the proton exchanged phase modulator in single-crystal lithium niobate thin film. *Opt. Express* **2016**, *24*, 257323. [[CrossRef](#)]
13. Camlibel, I. Spontaneous polarization measurements in several ferroelectric oxides using a pulsed-field method. *J. Appl. Phys.* **1969**, *40*, 1690. [[CrossRef](#)]
14. Zhang, H.H.; Zhu, H.B.; Li, Q.Y.; Hu, H. Reversed domains in x-cut lithium niobate thin films. *Opt. Mater.* **2020**, *109*, 110364. [[CrossRef](#)]
15. Gui, L. Periodically Poled Ridge Waveguides and Photonic Wires in  $\text{LiNbO}_3$  for Efficient Nonlinear Interactions. Ph.D. Thesis, University of Paderborn, Paderborn, Germany, 2010; pp. 41, 83.
16. Chang, L.; Li, Y.F.; Volet, N.; Wang, L.R.; Peters, J.; Bowers, J.E. Thin film wavelength converters for photonic integrated circuits. *Optica* **2016**, *3*, 531–535. [[CrossRef](#)]
17. Li, X.J.; Terabe, K.; Hatano, H.; Zeng, H.R.; Kitamura, K. Domain patterning thin crystalline ferroelectric film with focused ion beam for nonlinear photonic integrated circuits. *J. Appl. Phys.* **2006**, *100*, 106103. [[CrossRef](#)]

18. Gao, R.H.; Yao, N.; Guan, J.L.; Deng, L.; Lin, J.T.; Wang, M.; Qiao, L.L.; Fang, W.; Cheng, Y. Lithium niobate microring with ultra-high Q factor above  $10^8$ . *Chin. Opt. Lett.* **2022**, *20*, 011902. [[CrossRef](#)]
19. Gao, R.H.; Zhang, H.S.; Bo, F.; Fang, W.; Hao, Z.Z.; Yao, N.; Lin, J.T.; Guan, J.L.; Deng, L.; Wang, M.; et al. Broadband highly efficient nonlinear optical processes in on-chip integrated lithium niobate microdisk resonators of Q-factor above  $10^8$ . *New J. Phys.* **2021**, *23*, 123027. [[CrossRef](#)]
20. Wu, C.C.; Horng, R.H.; Wu, D.S.; Chen, T.N.; HO, S.S.; Ting, C.J.; Tsai, H.Y. Thinning technology for lithium niobate wafer by surface activated bonding and chemical mechanical polishing. *Jpn. J. Appl. Phys.* **2006**, *45*, 3822–3827. [[CrossRef](#)]
21. Tomita, Y.; Sugimoto, M.; Eda, K. Direct bonding of LiNbO<sub>3</sub> single crystals for optical waveguides. *Appl. Phys. Lett.* **1995**, *66*, 1484–1485. [[CrossRef](#)]
22. Jia, Y.C.; Wang, L.; Chen, F. Ion-cut lithium niobate on insulator technology: Recent advances and perspectives. *Appl. Phys. Rev.* **2021**, *8*, 011307. [[CrossRef](#)]
23. Regener, R.; Sohler, W. Loss in low-finesse Ti: LiNbO<sub>3</sub> optical waveguide resonators. *Appl. Phys. B Lasers Opt.* **1985**, *36*, 143–147. [[CrossRef](#)]
24. Honardoost, A.; Safian, R.; Rao, A.; Fathpour, S. High-Speed Modeling of Ultracompact Electrooptic Modulators. *J. Lightwave Technol.* **2018**, *36*, 5893–5902. [[CrossRef](#)]
25. Boynton, N.; Cai, H.; Gehl, M.; Arterburn, S.; Dallo, C.; Pomerene, A.; Starbuck, A.; Hood, D.; Trotter, D.C.; Friedmann, T.; et al. A heterogeneously integrated silicon photonic/lithium niobate travelling wave electro-optic modulator. *Opt. Express* **2020**, *28*, 1868–1884. [[CrossRef](#)]
26. Sun, S.H.; He, M.B.; Xu, M.Y.; Gao, S.Q.; Chen, Z.Y.; Zhang, X.; Ruan, Z.L.; Wu, X.; Zhou, L.D.; Liu, L.; et al. Bias-drift-free Mach–Zehnder modulators based on a heterogeneous silicon and lithium niobate platform. *Photonics Res.* **2020**, *8*, 1958–1963. [[CrossRef](#)]
27. Yonekura, K.; Jin, L.H.; Takizawa, K. Measurement of dispersion of effective electro-optic coefficients  $r_{13}^E$  and  $r_{33}^E$  of non-doped congruent LiNbO<sub>3</sub> Crystal. *J. Appl. Phys.* **2008**, *47*, 5503–5508. [[CrossRef](#)]
28. Minakata, M.; Kumagai, K.; Kawakami, S. Lattice constant changes and electro-optic effects in proton-exchanged LiNbO<sub>3</sub> optical waveguides. *Appl. Phys. Lett.* **1986**, *49*, 992–994. [[CrossRef](#)]